The Role of Nanostructure Morphology of Nickel-Infused Alumina on Solar-Thermal Energy Conversion

Xuanjie Wang[1], Mei-Li Hsieh[2, 3], James A. Bur[2], Shawn-Yu Lin[2], Shankar Narayanan[1, *]

[1]Department of Mechanical, Aerospace and Nuclear Engineering,
Rensselaer Polytechnic Institute, 110 8th St., Troy, NY, 12180, United States.
[2]Department of Physics, Applied Physics and Astronomy,
Rensselaer Polytechnic Institute, 110 8th St., Troy, NY, 12180, United States.
[3]Department of Photonics, National Chiao-Tung University, Hsinchu City, Taiwan.
*Corresponding author: narays5@rpi.edu

Keywords:

Spectrally-Selective Solar Absorber, Solar Absorber, Solar-thermal energy conversion, Design of experiments, Full factorial design

Abstract:

Solar-thermal energy conversion can be useful in many applications, including water desalination, and thermal energy storage. In this regard, using spectrally-selective solar absorbers is vital due to their high solar absorptance and low thermal emittance. While selective absorbers can be created using a wide range of nanomaterials, the underlying geometry may control the overall performance of solar-thermal energy conversion. With different geometries, it is possible to obtain a wide range of optical responses ranging from broadband to selective absorption of light. In this study, we focus on the role of nanostructure morphology of nickel-infused alumina (Ni/NPA) based spectrally-selective solar absorbers. This study demonstrates the use of the design of experiments (DOE) to analyze the effect of various geometric factors on the resulting optical response of Ni/NPA in the context of solar-thermal energy conversion. We show how this approach can provide a unique insight into the role of various geometric factors on the solar absorptance and thermal emittance of Ni/NPA-based absorbers, and demonstrate how it can guide the development of spectrally-selective materials. We believe a similar approach can be useful in the development of other optical materials for different applications.

1 Introduction

Solar-thermal energy conversion can be useful in many applications, including power generation[1], water heating[2], steam generation[3], desalination[3], and thermal energy storage[4–7]. Consequently, several techniques have been explored to maximize the absorption of sunlight, which includes the use of natural wood coated with carbon[8–11], hydrogels with tailored surface topography[12], graphene

oxide[13–15], polymers[16,17], metal-oxides[18], three-dimensional graphene[19], exfoliated graphite[20], and plasmonic surfaces[21–24]. These techniques have a common objective of maximizing the absorption of light using a black surface.

Though a black absorber allows high solar absorptance, it also corresponds to a high thermal emittance, which can result in significant energy loss, especially with the use of solar concentration. Unlike broadband absorbers, materials showing wavelength-selective absorption, with strong solar absorptance but low thermal emittance, can be more beneficial. Figure 1 illustrates this point by superposing the terrestrial solar irradiance, blackbody emissive power at 100 ℃, and absorptance of an ideal selective absorber. While we choose 100 ℃ as a reference due to its relevance to steam generation at atmospheric pressure, with the use of a solar concentrator, the absorber temperature can be significantly higher.

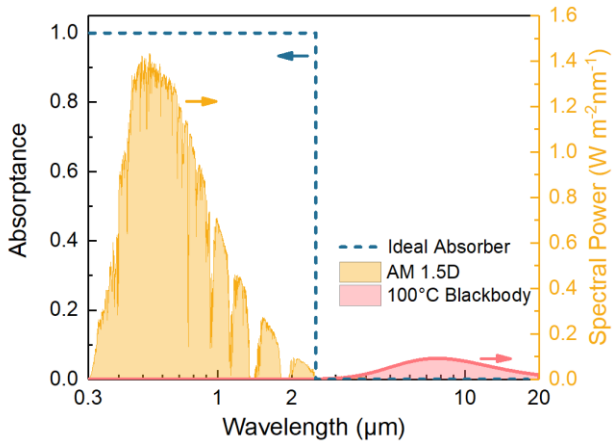

Figure 1. Spectral power corresponding to solar radiation at sea level and a blackbody at 100 ℃ (right y-axis). Spectral absorptance of an ideal selective absorber (left y-axis).

For a solar absorber, multiple modes of heat transfer can co-occur, and one of the ways to quantify performance is by determining the overall thermal efficiency, η as

$$\eta = [\alpha G - \varepsilon\sigma(T_s^4 - T_a^4) - H(T_s - T_a)]/G \tag{1}$$

where the average solar absorptance, α, and thermal emittance, ε of the absorber are given by

$$\alpha = \int_0^\infty \alpha_\lambda(T,\lambda) I_S \, d\lambda \Big/ \int_0^\infty I_S \, d\lambda \tag{2}$$

$$\varepsilon = \int_0^\infty \varepsilon_\lambda(T,\lambda)\, E_{b\lambda}(T,\lambda) d\lambda \Big/ \int_0^\infty E_{b\lambda}(T,\lambda) d\lambda \tag{3}$$

Here λ is the wavelength, and $\alpha_\lambda(T,\lambda)$ and $\varepsilon_\lambda(T,\lambda)$ are the spectral absorptance and emittance, respectively. I_S is the spectral solar irradiance and $E_{b\lambda}(T,\lambda)$ is the blackbody emissive power at wavelength, λ, and temperature, T.

Equation (1) shows that only a portion of total solar radiation (αG) is absorbed, where $G = \int_0^\infty I_S \, d\lambda$ is the net solar flux. Energy loss can occur via thermal emission, conduction, and

convective heat transfer, which depend on the surface and ambient temperatures, T_s and T_a, respectively. The rate of emissive loss per unit area of the solar absorber is $\varepsilon\sigma(T_s^4 - T_a^4)$, where ε is the average thermal emittance. The combined energy loss by conduction and convection, given by $H(T_{abs} - T_{amb})$, depends on H, the heat loss coefficient – a parameter that depends on various factors, including the materials and the design of the solar absorber.

It is clear that for a given H, we can improve η if the solar absorptance, α can be maximized, and the thermal emittance, ε can be minimized. This strategy, although less common, has been pursued with the use of gold nanoparticles[25], intrinsic absorbers[26,27], cermet-based absorbers[28–30], multilayer nanofilms[31,32] and photonic crystals[33–35]. However, the use of noble metals, intricate fabrication, and expensive materials make scalability a big challenge. Hence, widely-applicable spectrally-selective materials are desirable. The cermet-based absorbers, with metal nanoparticles embedded in a dielectric matrix, are reflective in the infrared region, while strongly absorbing in the visible wavelength region because of the interband transitions in the metal and plasmon resonances due to the metal nanoparticles. The plasmonic metal nanoparticles are attractive due to effective scattering, trapping and absorption of solar radiation. Nickel is chosen as the metal inclusion in the nanoporous alumina matrix by considering the optical properties[36], thermal stability[37–39] and significantly lower costs relative to noble metals. Hence, for the aforementioned reasons, this study analyzes the use of nickel-infused nanoporous alumina (Ni/NPA) as a low-cost, structurally stable, and spectrally-selective absorber.

Nanoporous alumina (NPA) has been used as a template to create nanostructures for many applications[40–53]. A few studies have also shown its use in creating wavelength-selective absorbers due to their excellent optical properties, scalability, and thermal stability[29,30,54–57]. However, since it is possible to create Ni/NPA with a wide range of nanostructure geometries, the resulting optical properties can vary significantly. Consequently, the most suitable geometry can be application-specific and would require a prudent selection strategy. This study demonstrates, for the first time, the use of the design of experiments (DOE) to analyze the effect of nanostructure morphology on the resulting optical properties of Ni/NPA. We show how this approach can provide a unique insight into the role of various geometric factors on the resulting solar absorptance and thermal emittance of Ni/NPA-based absorbers, and guide the development of spectrally-selective materials for solar-thermal energy conversion. Although we focus on Ni/NPA-based absorbers, we believe that a similar approach can be extended to other optical materials for different applications.

2 Fabrication of Ni/NPA Selective Absorbers

The Ni/NPA absorbers consist of three constituent materials, which are the nanoporous alumina (NPA), nickel nanowires (Ni-NWs) at the base of the nanopores, and the aluminum substrate, as shown in Figure 2. The fabrication of Ni/NPA-based selective absorber utilizes a two-step anodization process followed by nickel deposition using the pulse electrodeposition (PED) process, as described below.

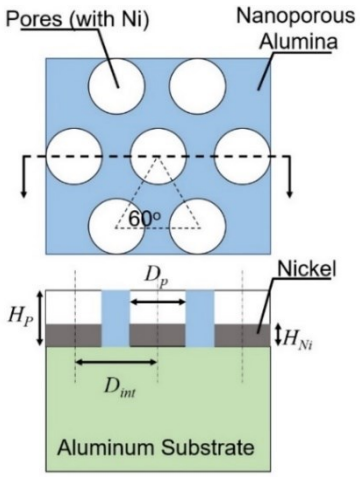

Figure 2. Top and cross-sectional views illustrating the characteristic geometry of nickel-infused nanoporous alumina (Ni/NPA).

The fabrication process uses aluminum foils (99.99 wt. % pure, Alfa Aesar Chemicals) of thickness 250 μm. The foil is degreased in acetone by ultrasonication for 20 minutes, followed by rinsing with isopropyl alcohol and deionized water. An aluminum etchant (H_3PO_4: HNO_3: CH_3COOH: H_2O = 80%:5%:5%:10%) at 40 ℃ for 2 minutes can deep clean the aluminum foil. Then electropolishing in perchloric acid-ethanol solution ($HClO_4$: C_2H_5OH = 1: 4) at 5 ℃ and 20 V for 90 s can provide a polished surface. Aluminum etching and electropolishing processes, although not essential, allows achieving a more ordered arrangement of nanopores. Subsequently, anodization in 0.3 M oxalic acid in a temperature-controlled (20 ℃) double-jacketed beaker for 30 minutes at 40 V creates NPA. The initial layer of NPA is etched away by placing the sample in a solution of phosphoric acid (6 wt. %), and chromic acid (1 wt. %) at 60 ℃ for 20 minutes, which leaves behind a uniform array of dimples on the aluminum surface. The second anodization process for 10 minutes at a constant potential of 40 V creates well-ordered NPA, which is followed by an exponentially decaying anodization potential to thin the barrier layer between the NPA and the aluminum substrate. A pore widening process by immersing the sample in a 5 wt.% phosphoric acid solution at 35 ℃ for 7 minutes enlarges the pore to the desired diameter. Nickel is then deposited in the NPA by a modified pulsed electrodeposition process. The process takes place with a deposition time of 5 ms at 5 V, and a relaxation time of 90 ms (0 V) in a Watts bath (300 g/L $NiSO_4$, 45 g/L $NiCl_2$, and 45 g/L H_3BO_3) at 40 ℃. After nickel disposition, a final etching process using 6 wt.% phosphoric acid and 1 wt.% chromic acid at 35 ℃ for 90 s removes some of the surface irregularities and shortens the NPA pores to obtain the desired pore height.

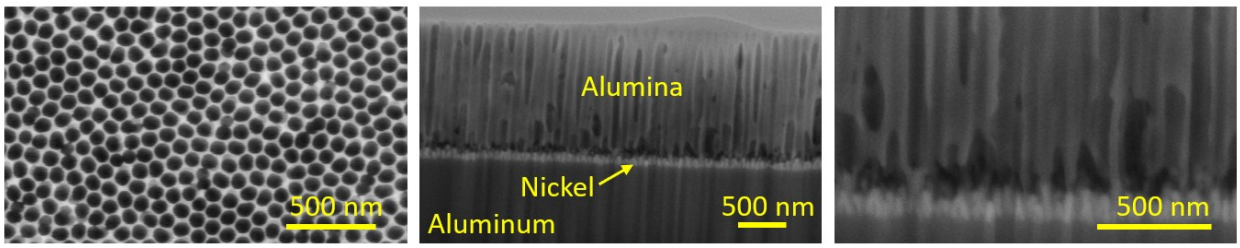

Figure 3. Top and cross-sectional views of fabricated Ni/NPA samples.

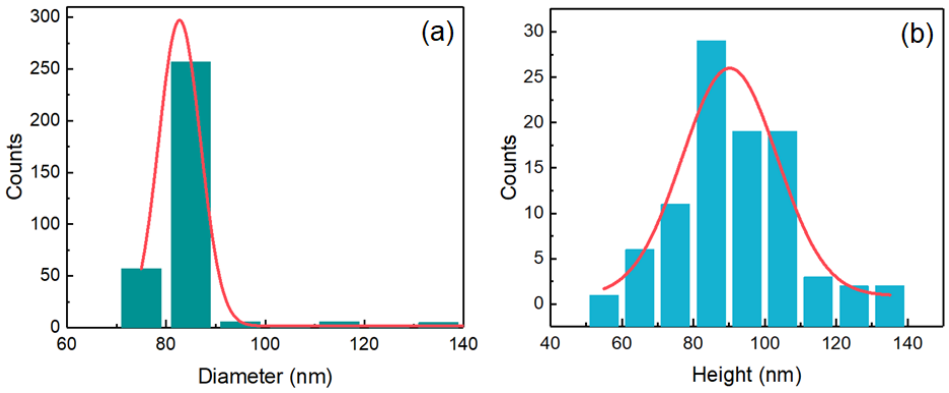

Figure 4. Image analysis of fabricated Ni/NPA sample to determine the distribution of (a) pore diameters, and (b) height of electro-deposited nickel.

The morphology of the Ni/NPA absorbers made using the process described above was characterized using high-resolution scanning electron microscopy (Zeiss 1540ESB Crossbeam FIB/SEM), as shown in Figure 3 (left). The morphology of Ni inside the nanopores was examined by the cross-sectional SEM image, as shown in Figure 3 (right). Image analysis of fabricated Ni/NPA samples then determine the distribution of pore diameters (D_p), and the height of electro-deposited nickel (H_{Ni}), as shown in Figure 4(a) and (b), respectively. In this case, $D_p = 83 \pm 4.5$ nm, $H_{Ni} = 90 \pm 15$ nm, $H_p = 1.4$ µm and $D_{int} = 110$ nm.

Several fabrication parameters, including the anodization temperature, voltage, duration, and pulse characteristics for nickel deposition, can alter the Ni/NPA's geometry. Prior studies on NPA fabrication show that the pore diameter and interpore distance are directly proportional to the anodization voltage[46,58]. For example, the increase in pore diameter with voltage for anodization in phosphoric acid is given by $\zeta_p = 1.29\ \text{nm V}^{-1}$. The interpore distance can be varied using mild (MA) and hard anodization (HA) in sulfuric, oxalic, selenic and phosphoric acid with a voltage dependence of $\zeta_{MA} = 2.5\ \text{nm V}^{-1}$ and $\zeta_{HA} = 1.8 - 2.0\ \text{nm V}^{-1}$, respectively[59,60]. A wet-chemical etching process using phosphoric acid widens the pore diameter at a rate of 1.04 nm min^{-1} at 29 °C [61]. Finally, the amount of nickel in the alumina nanopores can be controlled by the deposition current based on the Faraday's Law[62].

As such, a wide variety of Ni/NPA absorbers can be created with significantly different geometry, leading to different optical properties. Hence, in order to develop application-specific solar absorbers, a detailed computational analysis is necessary to understand the effect of the underlying geometry. This understanding can then guide the fabrication process to achieve the desired absorption characteristics.

3 Computational Prediction of Optical Response

The geometric parameters relevant to the Ni/NPA-based absorbers are the interpore distance (D_{int}), pore diameter (D_p), the height of AAO (H_p), and the height of nickel (H_{Ni}), as indicated in Figure 2. In this study, the computational prediction of optical response uses a finite element method to analyze the propagation of light through Ni/NPA by solving Maxwell's equations. This analysis conducted using Comsol Multiphysics predicts the transmission, reflection, and absorption of the incident light by obtaining the electric and magnetic field distribution across the

material[63]. Specifically, the computational model utilizes wavelength-dependent scattering parameters to determine the transmission and reflection of electromagnetic waves at different ports, where electromagnetic energy enters or exits the model. The reflection (R) and transmission (T), representing the rate of reflected and transmitted power, are obtained from the scattering parameters, which allows the calculation of spectral absorptance (A) based on $A = 1 - T - R$. In order to conduct this analysis, the computational model utilizes wavelength-dependent complex-valued refractive indices of the constituent materials for a given Ni/NPA geometry. For example, Figure 5 shows the spectral absorptance of Ni/NPA with $D_p = 80$ nm, $D_{int} = 110$ nm, $H_p = 2$ μm and $H_{Ni} = 120$ nm. As expected, the profile indicates wavelength-selective behavior, with larger absorptance in the visible and near infrared (IR) wavelengths and a lower absorptance for higher wavelengths.

Besides modeling, we also measure the diffuse reflectance, ρ_λ of the fabricated samples using a spectrometer (USB2000 interfaced with an Integrating Sphere, Ocean Optics) to quantify the performance of the absorbers, over a wavelength range of 400-1000 nm. To measure the reflectance in the IR wavelength range from 1 to 15 μm, we used a Fourier-transform infrared spectrometer (FTIR, Thermo Fisher Scientific) interfaced with a microscope (Nicolet Continuum, Thermo Fisher Scientific). In this case, a gold standard mirror normalizes the measured IR reflectance. Since the absorbers are made from relatively thick aluminum foils, they are all opaque, and the absorptance is inferred from the measurement of the reflectance as $\alpha_\lambda = 1 - \rho_\lambda$.

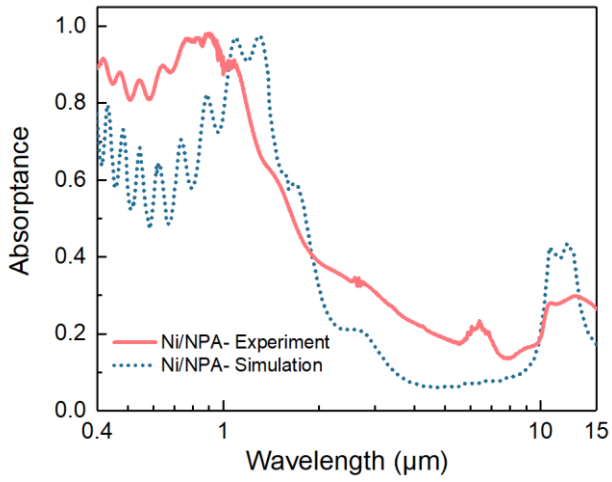

Figure 5. A comparison of calculated and experimentally characterized spectral absorptance of Ni/NPA sample with $D_p = 80$ nm, $D_{int} = 110$ nm, $H_p = 2$ μm and $H_{Ni} = 120$ nm.

Figure 5 compares the calculated and experimentally characterized spectral absorptance of the Ni/NPA sample with $D_p = 80$ nm, $D_{int} = 110$ nm, $H_p = 2$ μm and $H_{Ni} = 120$ nm. While there is a general agreement between the predictions and the measurements, there are some differences as well. Both indicate similar trends. In the visible spectrum, experiments and simulation results show an oscillatory behavior of the spectral absorptance. The strong absorptance is mainly due to the enhanced local surface plasmon resonance and interband transitions of nickel and aluminum[64]. The interband transition occurs around 1.4 and 1.5 eV in the dielectric function of nickel and aluminum, respectively, which correspond to the peak around 900 nm shown in Figure 5[65–67]. However, the

measured absorptance is higher. This difference is mainly due to the roughness and non-ideal geometry of the fabricated samples, which reduces the measured peak-to-peak amplitudes as well[68,69].

To compare the effects of each constituent material, Figure 6 shows the spectral absorptance of NPA, Ni nanowires, and Ni/NPA with $H_{Ni} = 100$ nm, $D_p = 80$ nm, $D_{int} = 100$ nm, and $H_p = 1000$ nm. The Ni nanowires show higher absorptance at lower wavelengths with a peak near 800 nm. The absorptance reduces significantly at higher wavelengths. The NPA geometry is generally reflective, and the absorptance spectrum shows an oscillatory behavior in the visible and near-IR wavelengths. In the IR wavelengths, the NPA shows a singular peak. The absorptance spectrum of Ni/NPA shows some similarities with NPA and Ni nanowires. It exhibits higher absorptance at lower wavelengths along with the presence of oscillations, and a lower absorptance at higher wavelengths. The higher absorption is attributed to the enhanced light-matter interaction among the cavities[70]. Like NPA, Ni/NPA also shows a peak value in absorptance in the IR region since the wavelength is much greater than the characteristic size of Ni nanostructures.

The use of detailed computational analysis is typical for quantifying the role of geometry and materials, which leads to the design of solar absorbers and reflectors. However, this approach helps in studying only one factor at a time. Consequently, it may require a significantly large number of computational runs to understand the role of geometric factors. Besides, it may still not identify how the selection of one geometric parameter could depend on the selection of another parameter. In order to address these issues, we carry out a design of experiments study, as described below, to guide the design of Ni/NPA solar absorbers.

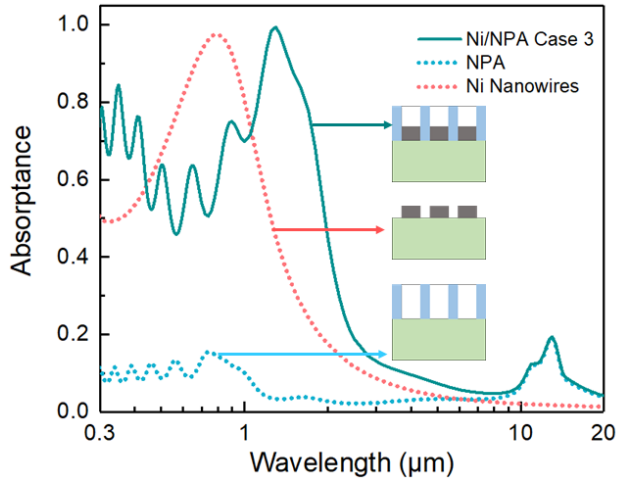

Figure 6. Spectral absorptance of nanostructures with comparable geometry. Here $H_{Ni} = 100$ nm, $D_p = 80$ nm, $D_{int} = 100$ nm, and $H_p = 1000$ nm.

4 Full Factorial Design of Ni/NPA Absorber

We conducted a full factorial design study to quantify the role of different geometric factors on the average solar absorptance (α) and thermal emittance (ε) of Ni/NPA. This study was carried out using a statistical software called Minitab[71]. The full factorial design considers two distinct

values or levels for each factor, H_{Ni}, D_p, D_{int} and H_p, and the resulting 2^4 combinations of these factors are listed as cases 1 to 16 in Table 1.

Table 1. Parametric combinations (cases 1 to 16) to study the effect of geometry on the optical response of Ni/NPA absorber. All geometric values are listed in nanometers (nm).

Factor/Case#	**1**	**2**	**3**	**4**	**5**	**6**	**7**	**8**
$\boldsymbol{H_{Ni}}$	100	500	100	500	100	500	100	500
$\boldsymbol{D_p}$	40	40	80	80	40	40	80	80
$\boldsymbol{D_{int}}$	100	100	100	100	200	200	200	200
$\boldsymbol{H_p}$	1000	1000	1000	1000	1000	1000	1000	1000
Factor/Case#	**9**	**10**	**11**	**12**	**13**	**14**	**15**	**16**
$\boldsymbol{H_{Ni}}$	100	500	100	500	100	500	100	500
$\boldsymbol{D_p}$	40	40	80	80	40	40	80	80
$\boldsymbol{D_{int}}$	100	100	100	100	200	200	200	200
$\boldsymbol{H_p}$	2000	2000	2000	2000	2000	2000	2000	2000

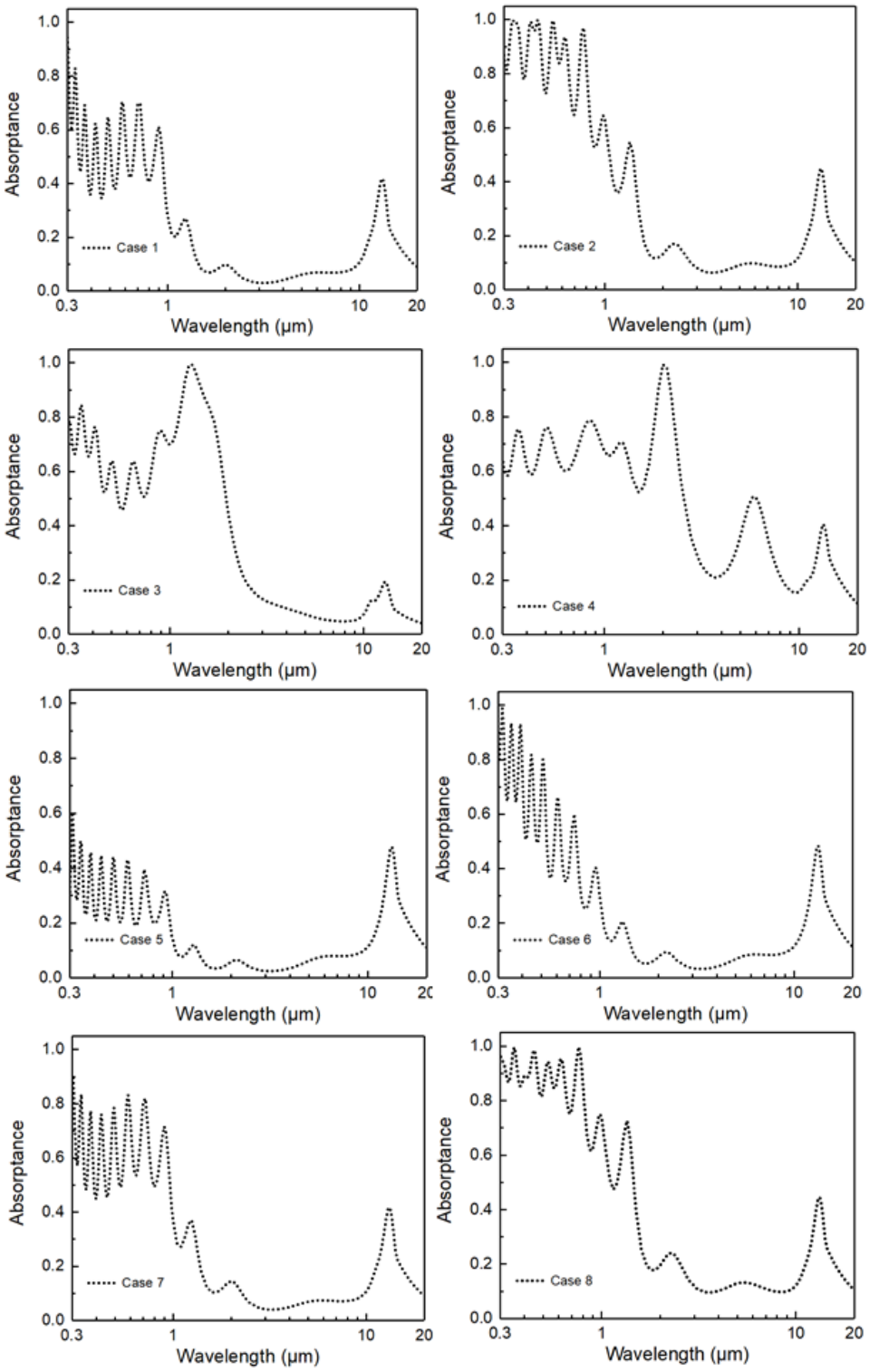

Figure 7. Spectral absorptance of Ni/NPA with geometries corresponding to cases 1 to 8 (see Table 1).

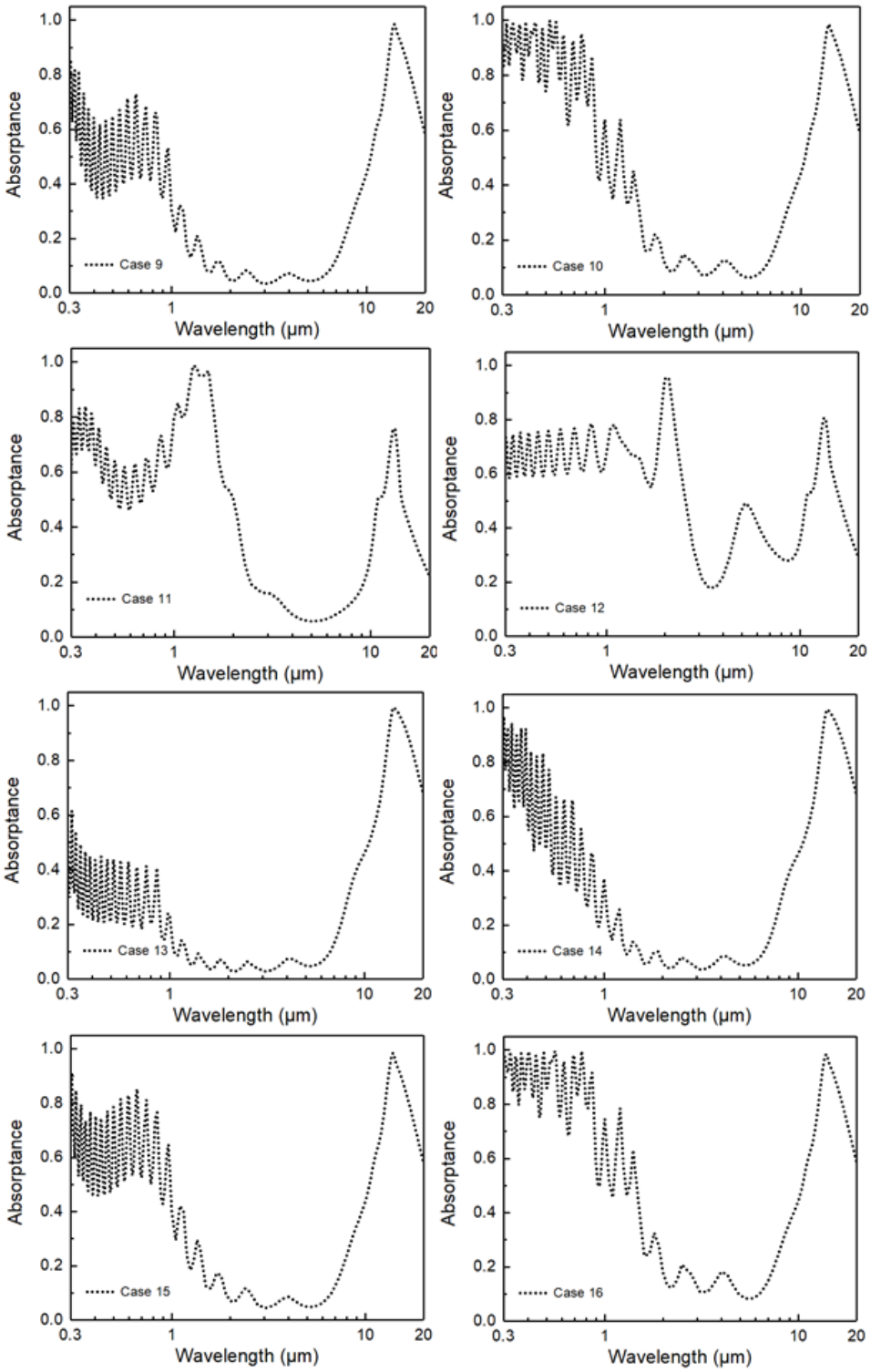

Figure 8. Spectral absorptance of Ni/NPA with geometries corresponding to cases 9 to 16 (see Table 1).

Figure 7 and Figure 8 show the spectral absorptance of Ni/NPA absorber for cases 1 to 8 and 9 to 16, respectively. In general, common characteristics and comparable trends can be identified. For example, cases 9 to 16 show the presence of a larger peak in the 10 to 20 μm wavelength range compared to cases 1 to 8. Matching trends can also be observed between any two cases, i and $i + 8$ due to the similar H_{Ni}, D_p and D_{int}, especially in the lower wavelengths (0.3 to 1 μm). However, each Ni/NPA geometry corresponds to a different optical response, resulting in a distinct average solar absorptance and thermal emittance.

Figure 9 shows the average solar absorptance and thermal emittance for different geometries, indicating that no two geometries result in similar performances. Cases 1 to 8 correspond to a lower ε compared to cases 9 to 16, due to a difference in H_p. Case 16 shows the highest α of 0.7364, and case 5 shows the lowest α of 0.2235. Similarly, case 14 shows the highest ε of 0.4751 and case 3 shows the lowest ε of 0.0816.

As the overall objective is to maximize the net energy absorbed from sunlight, it is worthwhile determining the net power, $\dot{Q}_{net}$ for different geometries. In this case, $\dot{Q}_{net}$ is calculated as $\dot{Q}_{net}/A = \alpha G - \varepsilon\sigma(T_s^4 - T_a^4)$. Note that this equation does not take into account the energy loss via convection and conduction modes of heat transfer since they depend on the system design, which can vary significantly with the application. We do this to focus mainly on the radiative heat transfer mechanism and avoid the complexities associated with the proper selection of H, the heat loss coefficient, which depends on the system design – as aspect outside the scope of this study. Here, the area A is 1 m^2, and the temperature of the surface, T_s, and the ambient temperature T_a is assumed as 100 ℃ and 20 ℃, respectively.

Figure 10 compares $\dot{Q}_{net}$ for different geometries. It is clear that the highest $\dot{Q}_{net}$ is neither case 16 (highest α) or case 3 (lowest ε). $\dot{Q}_{net}$ is maximum at 616 W for case 8, and minimum at -93 W for case 13, signifying a net energy loss to the environment from an absorber maintained at 100 ℃. The wide range of α, ε and $\dot{Q}_{net}$ obtained from various geometries is apparent in Figure 9 and Figure 10. Hence, quantifying the role of all geometric factors is essential, which is possible by comparing the main effects and interaction effects, as described below.

The full factorial analysis allows quantifying the effect of various factors in terms of main effects and interaction effects. In this regard, the main effects indicate the role of individual geometric parameters, and the interaction effects quantify the combined role of two or more geometric parameters. Figure 11 shows the main effects, which quantifies the individual roles of H_{Ni}, D_p, D_{int} and H_p on α and ε. Here, a main effect $\alpha(A)$ due to factor A among A, B, C and D, is calculated as

$$\alpha(\mathrm{A}) = \bar{\alpha}(\mathrm{A}+, \mathrm{B}, \mathrm{C}, \mathrm{D}) - \bar{\alpha}(\mathrm{A}-, \mathrm{B}, \mathrm{C}, \mathrm{D}) \tag{4}$$

where $A+$ and $A-$ denote the high and low levels of the factor A. $\bar{\alpha}(A+, B, C, D)$ is the average value of α computed for all level combinations of factors $A+$, B, C, and D. Similarly, $\bar{\alpha}(A-, B, C, D)$ is the average value of α computed for all level combinations of factors $A-$, B, C, and D. Note that all factors A, B, C, and D have high and low levels, as defined in Table 1. Likewise, the main effect, $\varepsilon(A)$ due to factor A among factors A, B, C, and D, is calculated as:

$$\varepsilon(\mathrm{A}) = \bar{\varepsilon}(\mathrm{A}+, \mathrm{B}, \mathrm{C}, \mathrm{D}) - \bar{\varepsilon}(\mathrm{A}-, \mathrm{B}, \mathrm{C}, \mathrm{D}) \tag{5}$$

In the range of geometries considered, Figure 11 shows that H_p plays a negligible role in controlling α. Among D_p, D_{int} and H_{Ni}, the largest effect on α is due to D_p, followed by H_{Ni} and D_{int}. On the other hand, H_p singlehandedly controls ε, followed by negligible contributions from H_{Ni}, D_p, and D_{int}. Apart from the main effects, α and ε may also dependent on the interaction effects, which measure the joint effects of two or more factors, as discussed below.

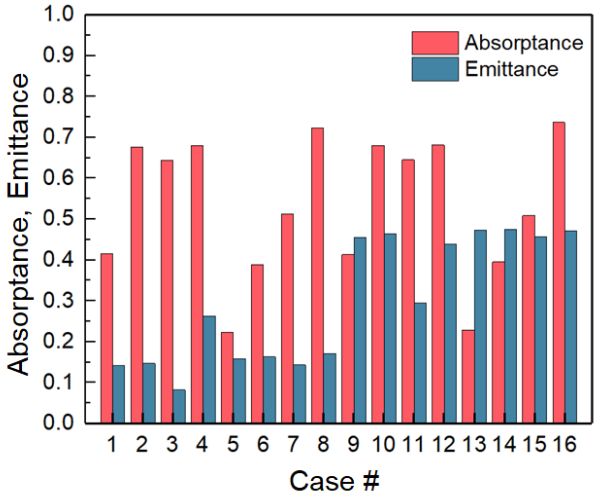

Figure 9. The average solar absorptance and thermal emittance of Ni/NPA surfaces at 100 ℃ with geometries corresponding to cases 1-16 (see Table 1).

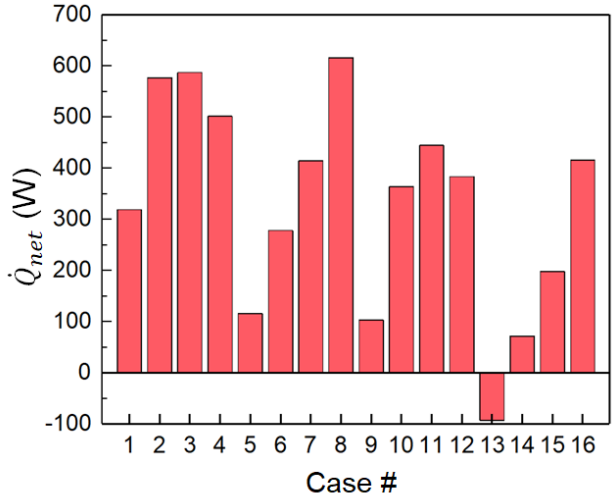

Figure 10. The net rate of energy absorbed by the Ni/NPA surface at 100 ℃ with geometries corresponding to cases 1-16 (see Table 1).

An interaction effect $\alpha(AB)$ indicates the joint effect of factors A and B on α. It is calculated as:

$$\alpha(AB) = \frac{1}{2}[\bar{\alpha}(A+,B+,C,D) + \bar{\alpha}(A-,B-,C,D)] - \frac{1}{2}[\bar{\alpha}(A+,B-,C,D) + \bar{\alpha}(A-,B+,C,D)] \quad (6)$$

Similarly, the interaction effect $\varepsilon(AB)$, which indicates the joint effect of factors A and B on ε, is calculated as:

$$\varepsilon(AB) = \frac{1}{2}[\bar{\varepsilon}(A+,B+,C,D) + \bar{\varepsilon}(A-,B-,C,D)] - \frac{1}{2}[\bar{\varepsilon}(A+,B-,C,D) + \bar{\varepsilon}(A-,B+,C,D)] \quad (7)$$

In general, a significant interaction effect, say $\alpha(AB)$, indicates that the effect of one factor on α, say A, depends on the value of the other factor, B, and vice versa. Figure 12 compares all the main and interaction effects affecting α and ε considering all factors A, B, C, and D, which denote H_p, D_{int}, D_p and H_{Ni}, respectively.

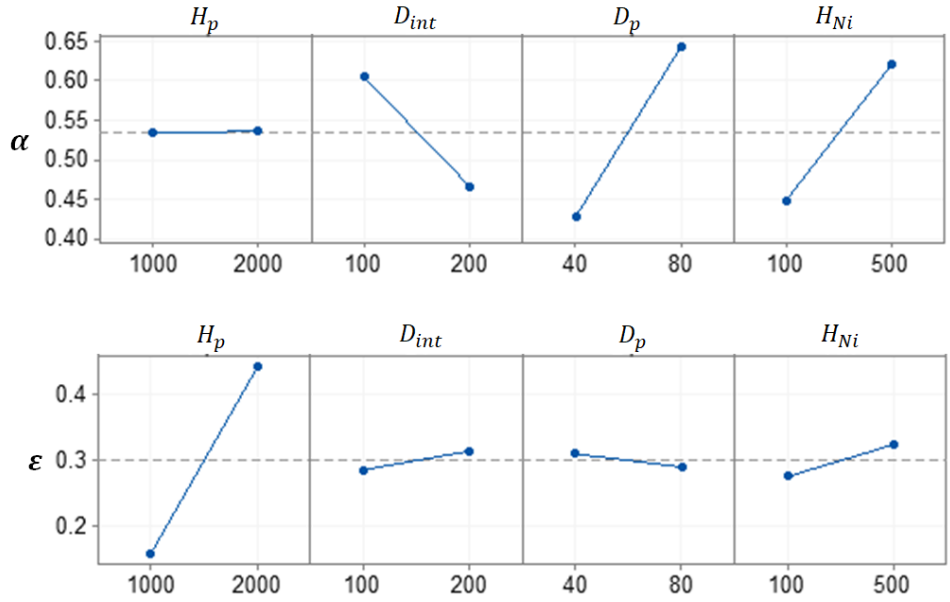

Figure 11. The average effect of individual geometric parameters (main effects) to solar absorptance (top) and thermal emittance (bottom) assuming Ni/NPA at 100 ℃.

With regards to their effects on α, Figure 12 shows that the four most important factors, in the decreasing order of importance, are D_p, H_{Ni}, D_{int}, and the interaction of D_p and D_{int}. With the interaction effect being significant, D_p and D_{int} cannot be chosen independently. As seen from the main effects plot (Figure 11), H_p is not an important parameter affecting α. Hence, if the overall objective is to control α, we need to carefully choose D_p, H_{Ni}, and D_{int}. Similarly, Figure 12 shows that the most important factor affecting ε is H_p. The next three important factors are H_{Ni}, followed by the interactions of factors D_p and H_{Ni}, and D_{int} and H_{Ni}. However, these effects are much smaller compared to H_p.

It is essential to understand the role of interaction effects, especially the effect of D_p and D_{int} interaction on α. Looking at the main effects alone, it would appear that α is higher for a larger D_p and a smaller D_{int}. However, this can be misleading since the largest and the second-largest values of α (cases 16 and 8) correspond to the higher value of D_{int} (200 nm). Note that cases 16 and 8 correspond to the higher value of D_p (80 nm) as well, and a combination of $D_{int} = 200$ nm and $D_p = 40$ nm (cases 5, 6, 13, and 14) typically results in the lowest possible values of α. We observe this response since the interaction effect of D_p and D_{int} is synergistic, which requires choosing higher values of D_{int} if D_p is also chosen at a higher level to maximize α. The role of the various interactions are shown in the two-dimensional plots in Figure 13 and Figure 14.

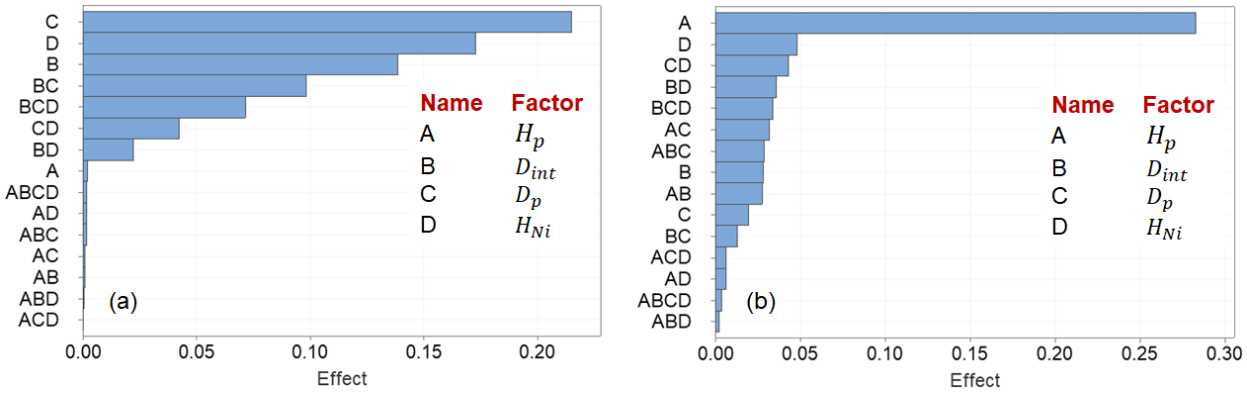

Figure 12. A quantitative comparison of the main effects and interaction effects of various factors on the average solar absorptance and thermal emittance of Ni/NPA surfaces at 100 °C.

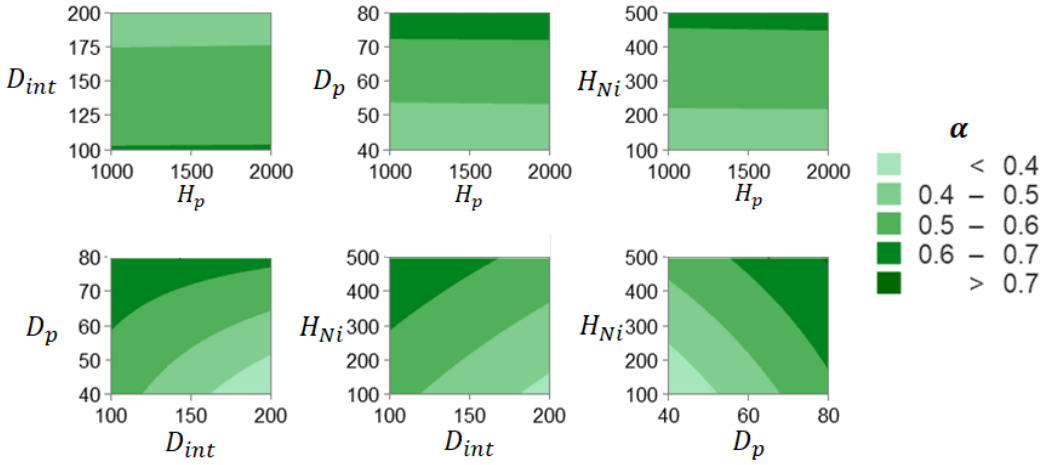

Figure 13. The effect of two-factor interactions on the average solar absorptance of the Ni/NPA surface. All geometric factors are shown in nanometers.

For the geometry analyzed in this study, Figure 13 and Figure 14 show how α and ε vary as a function of various geometric pairs among H_p, D_{int}, D_p and H_{Ni}. The two-dimensional contour plots are obtained by a regression analysis, which fits α and ε as a function of all the main and interaction effects. The plots also determine the values of H_p, D_{int}, D_p and H_{Ni} that could

potentially maximize α and minimize ε. Some aspects already discussed above are also apparent in these plots. For example, it is clear from Figure 13 (top row) that H_p does not affect α significantly. Similarly, it is clear from Figure 14 (top row) that H_p plays a very important role in controlling ε. Moreover, in order to obtain larger α, we should choose larger D_p and H_{Ni}. And since the interaction of D_p and D_{int} is statistically significant and synergistic, it is essential to select a larger D_{int} if a larger D_p is selected. Although H_{Ni}, D_{int}, and D_p also affect ε, their effect is significantly smaller compared to H_p. In general, Figure 13 and Figure 14 show that the selection of H_{Ni}, D_{int}, and D_p should be guided by the requirements for α, and the selection of H_p should be guided by the requirements for ε. Finally, although this approach guides the selection of Ni/NPA geometry to maximize energy absorption, it can also be extended to other geometries and materials. Since it allows quantifying the relative importance of different factors affecting the optical characteristics, it can be valuable in the design of efficient solar absorbers and reflectors.

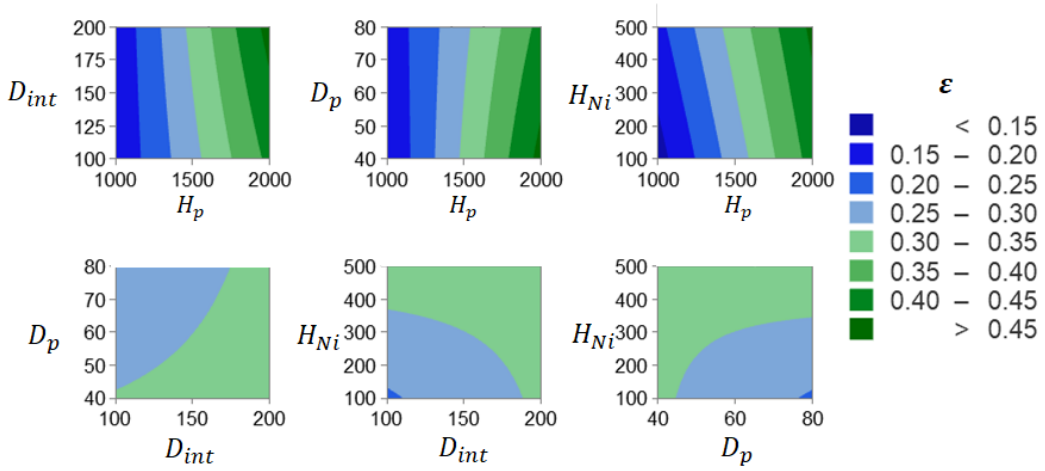

Figure 14. The effect of two-factor interactions on the average thermal emittance of the Ni/NPA surface maintained at 100 ℃. All geometric factors are shown in nanometers.

5 Conclusion

This study involves the development of nickel-nanoporous alumina (Ni/NPA) absorbers for efficient absorption of sunlight, which can be useful in various applications, including solar steam generation, thermal energy storage, and solar-thermal desalination. We note that for any given system incorporating solar absorbers, several modes of energy transfer mechanisms exist. The two prominent mechanisms analyzed in this study are the absorption of solar radiation and thermal emission. Efficient solar absorbers should exhibit a high solar absorptance, α, and a low thermal emittance, ε, in order to absorb and retain the maximum amount of energy. However, several factors can affect solar absorptance and thermal emittance, and in the context of Ni/NPA absorbers, geometry plays a crucial role. For Ni/NPA absorbers, which have an ordered array of nanostructures, four geometric parameters control its optical properties, which include the pore height H_p, the height on nickel inclusion in the nanopore, H_{Ni}, the interpore distance D_{int} and the pore diameter, D_p. We solve Maxwell's equations to predict the spectral absorptance of Ni/NPA for a given geometry, which allows the calculation of the average solar absorptance and thermal emittance, assuming an absorber temperature of 100 ℃. Since several geometric combinations are

possible, this study uses the design of experiments to compare the effects of various geometric parameters. We note that in the case of Ni/NPA absorbers the factors that affect α, in the decreasing order of importance are D_p, H_{Ni}, and D_{int}. The factor that affects ε is mainly H_p. Besides, we also note that geometric parameters cannot be picked independently since the choice of one parameter may depend on another. In this case, the choice of D_p and D_{int} are interdependent. In order to improve the net energy absorbed by Ni/NPA absorbers, it is necessary to minimize H_p, maximize D_p, D_{int} and H_{Ni}. Finally, we found that the use of the design of experiments as a tool to analyze the performance of solar absorbers adds significant value because it quantifies the role of various factors with manageable experiments and computational runs. Such an approach can be readily extended to develop solar materials for different applications.

6 Acknowledgements

S. Narayanan acknowledges the startup support from Rensselaer Polytechnic Institute and the support from the National Science Foundation's Division of Chemical, Bioengineering, Environmental, and Transport Systems in the Directorate for Engineering under Grant No. 1944323.

7 References

1. Hu, E., Yang, Y. P., Nishimura, A., Yilmaz, F. & Kouzani, A. Solar thermal aided power generation. *Appl. Energy* **87**, 2881–2885 (2010).
2. Kalogirou, S. A. *Solar thermal collectors and applications*. *Progress in Energy and Combustion Science* vol. 30 (2004).
3. Neumann, O. *et al.* Solar vapor generation enabled by nanoparticles. *ACS Nano* **7**, 42–49 (2013).
4. Hasnain, S. M. Review on sustainable thermal energy storage technologies, part I: Heat storage materials and techniques. *Energy Convers. Manag.* **39**, 1127–1138 (1998).
5. Narayanan, S. *et al.* Design and optimization of high performance adsorption-based thermal battery. in *ASME 2013 Heat Transfer Summer Conf. Collocated with the ASME 2013 7th Int. Conf. on Energy Sustainability and the ASME 2013 11th Int. Conf. on Fuel Cell Science, Engineering and Technology, HT 2013* vol. 1 (2013).
6. Narayanan, S. *et al.* A thermophysical battery for storage-based climate control. *Appl. Energy* **189**, (2017).
7. Narayanan, S. *et al.* Thermal battery for portable climate control. *Appl. Energy* **149**, 104-s116 (2015).
8. Chen, C. *et al.* Highly Flexible and Efficient Solar Steam Generation Device. *Adv. Mater.* **29**, 1701756 (2017).
9. Zhu, M. *et al.* Tree-Inspired Design for High-Efficiency Water Extraction. *Adv. Mater.* **29**, 1704107 (2017).
10. Zhu, M. *et al.* Plasmonic Wood for High-Efficiency Solar Steam Generation. *Adv. Energy Mater.* **8**, 1701028 (2018).

11. He, S. *et al.* Nature-inspired salt resistant bimodal porous solar evaporator for efficient and stable water desalination. *Energy Environ. Sci.* **12**, 1558–1567 (2019).

12. Guo, Y., Zhao, F., Zhou, X., Chen, Z. & Yu, G. Tailoring Nanoscale Surface Topography of Hydrogel for Efficient Solar Vapor Generation. *Nano Lett.* **19**, 2530–2536 (2019).

13. Li, Y. *et al.* Graphene oxide-based evaporator with one-dimensional water transport enabling high-efficiency solar desalination. *Nano Energy* **41**, 201–209 (2017).

14. Huang, L., Pei, J., Jiang, H. & Hu, X. Water desalination under one sun using graphene-based material modified PTFE membrane. *Desalination* **442**, 1–7 (2018).

15. Hong, Z. *et al.* Characteristics of the direct absorption solar collectors based on reduced graphene oxide nanofluids in solar steam evaporation. *Energy Convers. Manag.* **199**, 112019 (2019).

16. Kashyap, V. *et al.* A flexible anti-clogging graphite film for scalable solar desalination by heat localization. *J. Mater. Chem. A* **5**, 15227–15234 (2017).

17. Zhou, X., Zhao, F., Guo, Y., Zhang, Y. & Yu, G. A hydrogel-based antifouling solar evaporator for highly efficient water desalination. *Energy Environ. Sci.* **11**, 1985–1992 (2018).

18. Wang, J. *et al.* High-Performance Photothermal Conversion of Narrow-Bandgap Ti 2 O 3 Nanoparticles. *Adv. Mater.* **29**, 1603730 (2017).

19. Zhang, P. *et al.* Three-dimensional water evaporation on a macroporous vertically aligned graphene pillar array under one sun. *J. Mater. Chem. A* **6**, 15303–15309 (2018).

20. Sajadi, S. M., Farokhnia, N., Irajizad, P., Hasnain, M. & Ghasemi, H. Flexible artificially-networked structure for ambient/high pressure solar steam generation. *J. Mater. Chem. A* **4**, 4700–4705 (2016).

21. Gao, M., Connor, P. K. N. & Ho, G. W. Plasmonic photothermic directed broadband sunlight harnessing for seawater catalysis and desalination. *Energy Environ. Sci.* **9**, 3151–3160 (2016).

22. Zhou, L. *et al.* 3D self-assembly of aluminium nanoparticles for plasmon-enhanced solar desalination. *Nat. Photonics* **10**, 393–398 (2016).

23. Zhang, L. *et al.* Plasmonic heating from indium nanoparticles on a floating microporous membrane for enhanced solar seawater desalination. *Nanoscale* **9**, 12843–12849 (2017).

24. Chen, C. *et al.* Dual functional asymmetric plasmonic structures for solar water purification and pollution detection. *Nano Energy* **51**, 451–456 (2018).

25. Zhou, L. *et al.* Self-assembled spectrum selective plasmonic absorbers with tunable bandwidth for solar energy conversion. *Nano Energy* **32**, 195–200 (2017).

26. Randich, E. & Pettit, R. B. Solar selective properties and high temperature stability of CVD ZrB2. *Sol. Energy Mater.* **5**, 425–435 (1981).

27. Kennedy, C. Review of mid-to high-temperature solar selective absorber materials. *NREL Tech. Rep.* 1–58 (2002) doi:10.2172/15000706.

28. Ni, G. *et al.* Steam generation under one sun enabled by a floating structure with thermal

concentration. *Nat. Energy* **1**, 16126 (2016).

29. Cao, F., McEnaney, K., Chen, G. & Ren, Z. A review of cermet-based spectrally selective solar absorbers. *Energy Environ. Sci.* **7**, 1615 (2014).

30. Cao, F. *et al.* A high-performance spectrally-selective solar absorber based on a yttria-stabilized zirconia cermet with high-temperature stability. *Energy Environ. Sci.* **8**, 3040–3048 (2015).

31. Wang, H., Alshehri, H., Su, H. & Wang, L. Design, fabrication and optical characterizations of large-area lithography-free ultrathin multilayer selective solar coatings with excellent thermal stability in air. *Sol. Energy Mater. Sol. Cells* **174**, 445–452 (2018).

32. Li, Y. *et al.* Scalable all-ceramic nanofilms as highly efficient and thermally stable selective solar absorbers. *Nano Energy* **64**, 103947 (2019).

33. Rinnerbauer, V. *et al.* Recent developments in high-temperature photonic crystals for energy conversion. *Energy Environ. Sci.* **5**, 8815–8823 (2012).

34. Li, P. *et al.* Large-Scale Nanophotonic Solar Selective Absorbers for High-Efficiency Solar Thermal Energy Conversion. *Adv. Mater.* **27**, 4585–4591 (2015).

35. Khodasevych, I. E., Wang, L., Mitchell, A. & Rosengarten, G. Micro- and Nanostructured Surfaces for Selective Solar Absorption. *Adv. Opt. Mater.* **3**, 852–881 (2015).

36. Chen, M. *et al.* A Scalable Dealloying Technique To Create Thermally Stable Plasmonic Nickel Selective Solar Absorbers. *ACS Appl. Energy Mater.* **2**, 6551–6557 (2019).

37. Chen, M. & He, Y. Plasmonic nanostructures for broadband solar absorption based on the intrinsic absorption of metals. *Sol. Energy Mater. Sol. Cells* **188**, 156–163 (2018).

38. Karmhag, R., Niklasson, G. A. & Nygren, M. Oxidation kinetics of nickel nanoparticles. *J. Appl. Phys.* **89**, 3012–3017 (2001).

39. Unutulmazsoy, Y., Merkle, R., Fischer, D., Mannhart, J. & Maier, J. The oxidation kinetics of thin nickel films between 250 and 500 °c. *Phys. Chem. Chem. Phys.* **19**, 9045–9052 (2017).

40. Masuda, H. & Fukuda, K. Ordered Metal Nanohole Arrays Made by a Two-Step Replication of Honeycomb Structures of Anodic Alumina. *Science (80-.).* **268**, 1466–1468 (1995).

41. Masuda, H., Yotsuya, M. & Ishida, M. Spatially Selective Metal Deposition into a Hole-Array Structure of Anodic Porous Alumina Using a Microelectrode. *Jpn. J. Appl. Phys.* **37**, L1090–L1092 (1998).

42. Asoh, H. *et al.* Photonic Crystal Using Anodic Porous Alumina. *Jpn. J. Appl. Phys.* **38**, L1403–L1405 (2002).

43. Narayanan, S., Fedorov, A. G. & Joshi, Y. K. On-chip thermal management of hotspots using a perspiration nanopatch. *J. Micromechanics Microengineering* **20**, (2010).

44. Wang, X., Hsieh, M.-L., Bur, J. A., Lin, S.-Y. & Narayanan, S. Capillary-driven solar-thermal water desalination using a porous selective absorber. *Mater. Today Energy* **17**, 100453 (2020).

45. Wang, X. *et al.* Nickel-Infused Nanoporous Alumina as Tunable Solar Absorber. *MRS Adv.*

1–9 (2020) doi:10.1557/adv.2020.300.

46. Sousa, C. T. *et al.* Nanoporous alumina as templates for multifunctional applications. *Appl. Phys. Rev.* **1**, (2014).

47. Piao, Y., Lim, H., Chang, J. Y., Lee, W.-Y. & Kim, H. Nanostructured materials prepared by use of ordered porous alumina membranes. *Electrochim. Acta* **50**, 2997–3013 (2005).

48. Nagaura, T., Takeuchi, F. & Inoue, S. Fabrication and structural control of anodic alumina films with inverted cone porous structure using multi-step anodizing. *Electrochim. Acta* **53**, 2109–2114 (2008).

49. Masuda, H. & Satoh, M. Fabrication of Gold Nanodot Array Using Anodic Porous Alumina as an Evaporation Mask. *Jpn. J. Appl. Phys.* **35**, L126–L129 (1996).

50. Masuda, H. *et al.* Highly ordered nanochannel-array architecture in anodic alumina. *Appl. Phys. Lett.* **71**, 2770–2772 (1997).

51. Wang, G. *et al.* Robust superhydrophobic surface on Al substrate with durability, corrosion resistance and ice-phobicity. *Sci. Rep.* **6**, 20933 (2016).

52. Huang, C. F., Lin, Y., Shen, Y. K. & Fan, Y. M. Optimal processing for hydrophobic nanopillar polymer surfaces using nanoporous alumina template. *Appl. Surf. Sci.* **305**, 419–426 (2014).

53. Wu, J.-T., Chang, W.-Y. & Yang, S.-Y. Fabrication of a nano/micro hybrid lens using gas-assisted hot embossing with an anodic aluminum oxide (AAO) template. *J. Micromechanics Microengineering* **20**, 075023 (2010).

54. Boström, T., Westin, G. & Wäckelgård, E. Optimization of a solution-chemically derived solar absorbing spectrally selective surface. *Sol. Energy Mater. Sol. Cells* **91**, 38–43 (2007).

55. Salmi, J., Bonino, J. P. & Bes, R. S. Nickel pigmented anodized aluminum as solar selective absorbers. *J. Mater. Sci.* **35**, 1347–1351 (2000).

56. Li, L. AC anodization of aluminum, electrodeposition of nickel and optical property examination. *Sol. Energy Mater. Sol. Cells* **64**, 279–289 (2000).

57. Li, Z., Zhao, J. & Ren, L. Aqueous solution-chemical derived Ni–Al2O3 solar selective absorbing coatings. *Sol. Energy Mater. Sol. Cells* **105**, 90–95 (2012).

58. Hwang, S.-K., Jeong, S.-H., Hwang, H.-Y., Lee, O.-J. & Lee, K.-H. Fabrication of highly ordered pore array in anodic aluminum oxide. *Korean J. Chem. Eng.* **19**, 467–473 (2002).

59. O'SULLIVAN JP & WOOD GC. The morphology and mechanism of formation of porous anodic films on aluminium. *Proc. R. Soc. London. A. Math. Phys. Sci.* **317**, 511–543 (1970).

60. Lee, W. & Park, S.-J. Porous Anodic Aluminum Oxide: Anodization and Templated Synthesis of Functional Nanostructures. *Chem. Rev.* **114**, 7487–7556 (2014).

61. Han, H. *et al.* In Situ Determination of the Pore Opening Point during Wet-Chemical Etching of the Barrier Layer of Porous Anodic Aluminum Oxide: Nonuniform Impurity Distribution in Anodic Oxide. *ACS Appl. Mater. Interfaces* **5**, 3441–3448 (2013).

62. Sousa, C. T. *et al.* Tunning pore filling of anodic alumina templates by accurate control of the bottom barrier layer thickness. *Nanotechnology* **22**, 315602 (2011).

63. Comsol Multiphysics. https://www.comsol.com/.

64. Wang, X., Li, H., Yu, X., Shi, X. & Liu, J. High-performance solution-processed plasmonic Ni nanochain-Al 2O3 selective solar thermal absorbers. *Appl. Phys. Lett.* **101**, 1–6 (2012).

65. Kirillova, M. M. Electron Interband Transitions in Nickel. *J. Exp. Theor. Phys.* **34**, 178–182 (1972).

66. Pakizeh, T. Optical absorption of plasmonic nanoparticles in presence of a local interband transition. *J. Phys. Chem. C* **115**, 21826–21831 (2011).

67. Schuermans, S., Maurer, T., Martin, J., Moussy, J.-B. & Plain, J. Plasmon / interband transitions coupling in the UV from large scale nanostructured Ni films. *Opt. Mater. Express* **7**, 1787 (2017).

68. Yang, Z. P., Ci, L., Bur, J. A., Lin, S. Y. & Ajayan, P. M. Experimental observation of an extremely dark material made by a low-density nanotube array. *Nano Lett.* **8**, 446–451 (2008).

69. Chung, Y. C. *et al.* Surface roughness effects on aluminium-based ultraviolet plasmonic nanolasers. *Sci. Rep.* **7**, 1–9 (2017).

70. Mandal, J. *et al.* Scalable, "Dip-and-Dry" Fabrication of a Wide-Angle Plasmonic Selective Absorber for High-Efficiency Solar–Thermal Energy Conversion. *Adv. Mater.* **29**, 1–9 (2017).

71. Minitab. https://www.minitab.com/en-us/.